Sensors and Materials, Vol. 38, No. 6 (2026) 2977–2994
MYU Tokyo

S & M 4481

Affordable IoT Embedded System for Lateral Displacement Measurement Based on Active Moiré Patterns

Edgardo Tomás-Martínez,[1] José de Jesús Agustin Flores-Cuautle,[2]
Sulpicio Sánchez Tizapa,[1] Antonio Alarcón Paredes,[3] and Gustavo A. Alonso-Silverio[1*]

[1]Facultad de Ingeniería, Universidad Autónoma de Guerrero, Chilpancingo 39079, Guerrero, Mexico
[2]Secihti/Tecnológico Nacional de México/I.T., Orizaba, Veracruz 94300, Mexico
[3]Centro de Investigación en Computación, Instituto Politécnico Nacional, Mexico City 07738, Mexico

(Received February 20, 2026; accepted April 27, 2026)

Keywords: displacement measurement, Moiré pattern, embedded system, optical metrology, experimental mechanics

Noncontact displacement measurement is widely used in experimental mechanics; however, many optical techniques rely on high-end imaging hardware and external computing resources, limiting their applicability in low-cost laboratory setups. In this paper, we present a compact, affordable (<USD 240) embedded system for lateral displacement measurement based on active Moiré patterns, integrating a mini projector, a camera, and a Raspberry Pi platform acting as an IoT edge node for wireless data transmission. The system estimates displacement through image-based analysis, utilizing both spatial and reference-based empirical calibration against a physical grating to mitigate optical distortions. Experimental validation was performed for lateral displacements in the range of 0–12 mm using a digital indicator as a reference. The results show a consistent linear response with a correlation coefficient of 0.98, a mean absolute error of 0.207 mm, a root mean square error of 0.235 mm, and a mean standard deviation of 0.033 mm across repeated measurements. Rather than competing directly with state-of-the-art Moiré approaches that demand high-end industrial cameras and sub-micrometer precision, we prioritize affordability, versatility, and real-world deployability. The main contribution of this work lies in providing an accessible IoT edge architecture capable of modernizing legacy manual equipment in resource-limited or educational laboratories. The achieved 0.2 mm resolution is demonstrated to be robust and sufficient for automated, quasi-static displacement monitoring in practical compression testing scenarios, effectively bridging the gap between advanced optical metrology and low-cost industrial monitoring.

1. Introduction

Accurate displacement measurement plays a central role in experimental mechanics, structural health monitoring, and geotechnical testing. As noted by Daras *et al.*[(1)] and Wang *et al.*,[(2)] conventional contact sensors such as linear variable differential transformers, strain

*Corresponding author: e-mail: gsilverio@uagro.mx
https://doi.org/10.18494/SAM6298

ISSN 0914-4935
https://myukk.org/

gauges, and displacement transducers provide high accuracy but require physical attachment, careful alignment, and extensive wiring, complicating their deployment in small specimens or harsh experimental environments. These limitations have motivated the development of noncontact optical methods capable of delivering reliable displacement measurements with reduced instrumentation complexity.

Vision-based techniques such as digital image correlation (DIC), particle image velocimetry, and photogrammetry have matured significantly over the past two decades, enabling full-field displacement and strain measurements under laboratory and field conditions.[3–5] However, Belloni *et al.*[6] and Jiang[7] reported that while these approaches provide rich spatial information and flexibility, they often rely on high-resolution imaging hardware and external computational resources, which constrains their applicability in compact, low-cost, or embedded experimental setups.

Within the family of optical methods, Moiré-based techniques offer an inherent displacement magnification mechanism. When two periodic patterns with slightly different pitches are superimposed, small relative shifts are converted into large-scale fringe movements whose phase is proportional to the underlying displacement. This magnification principle has been successfully exploited to detect microscale deformations, vibrations, and shape changes with subpixel sensitivity, as demonstrated by Saveljev and Kim,[8] Wang *et al.*,[9] and Chen *et al.,*[10] Furthermore, Dirckx[11] showed that digital sampling and phase-based Moiré approaches have further improved robustness and accuracy, enabling applications ranging from material testing to crack detection and vibration monitoring. However, many Moiré-based measurement systems are implemented using laboratory-grade optical setups and, as observed by Saveljev and Heo,[12] are primarily optimized for micro- or nanoscale deformation analysis, limiting their direct applicability to moderate displacement ranges encountered in routine compression testing.

Recent sampling Moiré approaches have demonstrated very high deformation-measurement accuracy using only a camera and a grating marker, achieving resolutions on the order of 1/100 to 1/1000 of the grating pitch (e.g., 0.02 mm).[13,14] While these methods represent highly relevant benchmarks for modern Moiré metrology, their peak performance intrinsically relies on high-resolution industrial cameras, highly controlled uniform laboratory illumination, and precision-manufactured grating tapes or specialized target materials.[14] Furthermore, recent field applications show that such extreme precision requires expensive high-megapixel sensors and specialized lighting, increasing overall costs and restricting their ease of deployment in budget-constrained settings.

In parallel, the availability of low-cost embedded computing platforms has opened new possibilities for autonomous and portable measurement systems. Single-board computers such as Raspberry Pi provide sufficient processing power to execute real-time image processing while remaining inexpensive and energy-efficient. Several studies, including those by Schlobohm *et al.*[15] and Wang and co-workers,[16,17] have demonstrated vision-based displacement measurement systems built around Raspberry Pi hardware for structural monitoring and laboratory instrumentation. Nevertheless, these systems commonly rely on template matching, DIC, or structured-light techniques and do not explicitly exploit Moiré-based displacement

magnification, nor are they optimized for the moderate displacement ranges typical of quasi-static compression testing.

As a result, there remains a practical gap in displacement measurement for laboratory-scale compression testing; that is, there is a lack of compact, low-cost systems capable of providing reliable, noncontact lateral displacement measurements in the moderate range (approximately 5–15 mm) using embedded hardware under standard laboratory conditions. Accordingly, to address this gap, the following contributions are primarily technological and application-oriented, focusing on democratizing optical metrology: (i) the integration of active Moiré projection, image acquisition, and on-board processing into a single, highly versatile, low-cost platform (<USD 240) designed specifically for educational and resource-limited laboratories; (ii) the implementation of an edge-computing workflow on a Raspberry Pi, eliminating the reliance on the expensive external desktop processing typically required by conventional high-end optical setups; and (iii) the robust incorporation of IoT functionality that enables real-time cloud data publication and remote supervision. Together, these elements define the novelty of the proposed system, demonstrating how accessible embedded hardware can retrofit legacy manual testing equipment and transition optical measurement from isolated laboratory benches to interconnected, real-world monitoring applications.

To validate this architecture, the system is experimentally tested for lateral displacements up to 12 mm using a digital indicator as a reference, enabling a direct comparison between image-based displacement estimation and independent physical measurement. A reference-based empirical calibration strategy is introduced to mitigate geometric distortions inherent to consumer-grade divergent optics. Experimental results demonstrate strong linearity ($R = 0.98$), a mean absolute error of 0.207 mm, a root mean square error (*RMSE*) of 0.235 mm, and a mean standard deviation of 0.033 mm, achieving sub-millimeter accuracy within the 0–12 mm displacement range. The extension of this approach to larger displacement ranges and fully automated testing scenarios remains beyond the scope of the present study and is left for future work.

2. Data, Materials, and Methods

2.1 System architecture

The projection unit consists of a commercial low-cost LED mini projector (Model: XuanPad V30), utilizing a liquid crystal display (LCD) with thin film transistor (TFT) technology, with a native resolution of 1920 × 1080 pixels, connected via a high-definition multimedia interface (HDMI), which projects the digitally generated fringe pattern onto the specimen surface. For the initial experimental validation, the physical grating, measuring 200 mm (width) × 140 mm (height), was printed and adhered to the front surface of a medium density fiberboard (MDF) specimen plate, where the actively analyzed region was defined by the overlapping central area, designated as the region of interest (ROI). This specific configuration demonstrates the system's ability to operate reliably with standard, readily available materials. Image acquisition is performed using a standard Steren Full HD USB webcam equipped with autofocus and a 75°

field of view, set to a resolution of 1920 × 1080 pixels and positioned perpendicular to the specimen to minimize perspective distortion and parallax effects, as shown in Fig. 1. The Raspberry Pi 4 Model B (4 GB RAM) acts as the central processing and control unit, executing custom Python scripts for system synchronization, image processing, and data logging. Additionally, the system operates as an IoT node by transmitting the computed displacement data asynchronously to a Firebase real-time database, enabling remote data monitoring. The total cost of the hardware components is approximately USD 240 (excluding the mounting structure), which represents a significant reduction compared with commercial DIC systems or high-end Moiré interferometers.

Prior to testing, the camera and projection units are rigidly mounted and kept fixed throughout the experiment. The x-axis is defined as the horizontal direction in the camera image plane and corresponds to the lateral displacement direction of interest during compression. All displacement measurements are referenced to an initial undeformed configuration acquired after the manual alignment of the projected and physical gratings.

In addition to local image processing, the Raspberry Pi operates as an IoT edge node for remote data logging and monitoring. The estimated displacement values are transmitted asynchronously via Wi-Fi to a cloud-based Firebase real-time database. Although the image processing pipeline runs continuously at approximately 15–20 frames per second (fps), cloud publication is performed at a reduced rate of 1 Hz, consistent with the quasi-static nature of the compression tests. The transmitted data corresponds to the temporally stabilized displacement output after application of the 10 s moving average filter. Measurements are simultaneously stored locally to ensure data integrity in case of network interruption. The cloud connection enables near real-time remote visualization and experiment supervision without affecting the displacement estimation algorithm. The proposed 'IoT-enabled system' functions as an edge-computing node: it acquires optical data locally, processes the Moiré interference measurements on-board (eliminating the need for expensive, dedicated desktop workstations), and wirelessly transmits the computed displacement values to a cloud-accessible database for remote visualization. This complete edge-to-cloud architecture is depicted in Fig. 2.

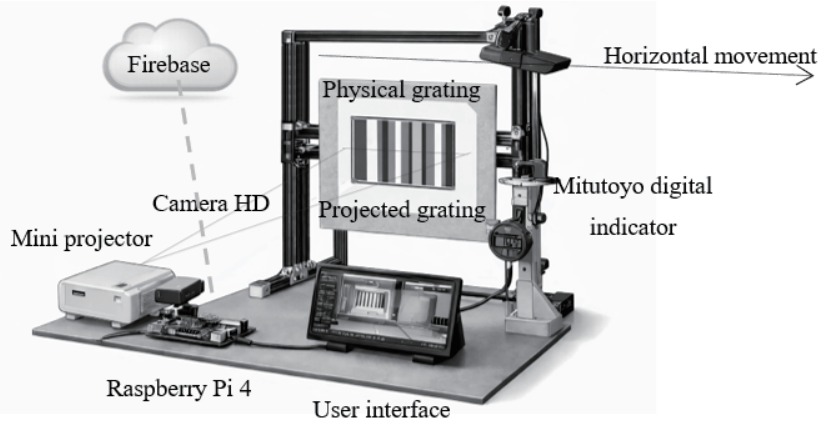

Fig. 1. Overall architecture of the embedded Moiré-based displacement measurement system.

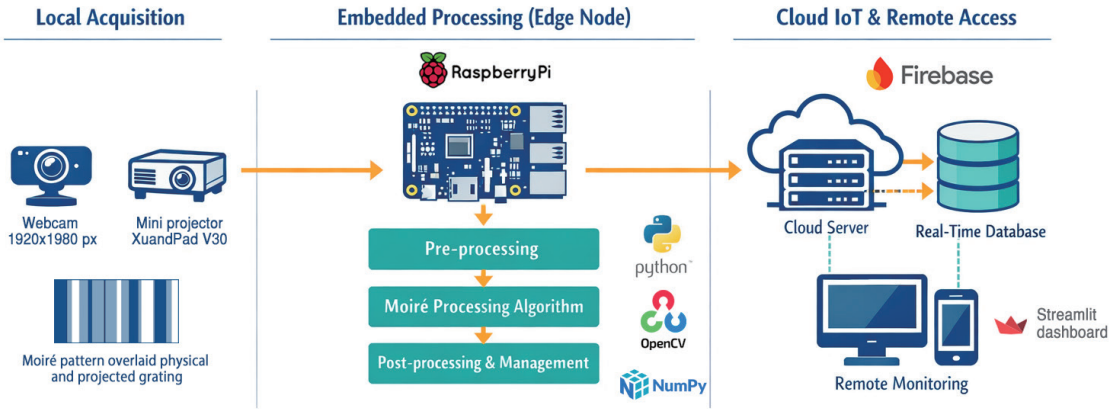

Fig. 2. (Color online) IoT architecture and edge-to-cloud system.

2.2 Grating design and active Moiré principle

The measurement principle is based on active Moiré interferometry using two gratings. The physical grating consists of a high-contrast pattern with a constant pitch p_g of 20 mm attached to the specimen surface. The digital grating is a software-generated sinusoidal fringe pattern with a slightly different pitch p_p of 26 mm at the specimen plane, which is projected and overlaid onto the same area to form Moiré fringes, as depicted in Fig. 3.

The selected grating pitches were chosen as a practical compromise between fringe magnification, visibility, and robustness under manual alignment. A physical grating pitch (p_g) of 20 mm ensures that individual grating lines remain clearly distinguishable by the webcam throughout the compression tests while maintaining a stable ROI. The projected grating was designed with a slightly larger pitch to satisfy the requirement for Moiré formation. A pitch mismatch of approximately 30% (between 20 and 26 mm) was found to provide an optimal balance: smaller mismatches increase theoretical magnification but are highly sensitive to illumination nonuniformity and alignment errors, whereas larger mismatches reduce Moiré amplification. The selected combination therefore enables stable Moiré fringe formation and reliable displacement tracking using low-cost hardware.

The pitch mismatch ($p_p \neq p_g$) between the physical and projected gratings produces large-scale Moiré fringes whose spatial period is governed by the difference in grating frequency (P_M).

$$P_M = (p_g \times p_p) / |p_g - p_p| \tag{1}$$

A small physical displacement (Δx) of the specimen causes a magnified shift of the Moiré fringes ($\Delta\varphi$), providing an optical amplification factor (P_M/p_g) that enhances measurement sensitivity. Since both gratings consist of parallel vertical bars, the resulting Moiré fringes exhibit predominant sensitivity to horizontal (x-axis) displacement, which is the primary quantity of interest in the present compression tests.

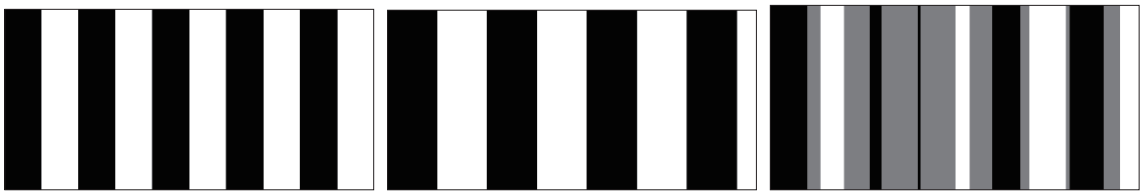

(a) (b) (c)

Fig. 3. (a) Physical grating black-on-white, pitch = 20 mm, (b) projected grating digitally generated, pitch = 26 mm, and (c) Moiré pattern overlaid on physical and projected gratings.

2.3 Image acquisition and ROI definition

Experiments were conducted under standard indoor lighting, without controlled illumination. Prior to data acquisition, the imaging system components of Raspberry Pi, camera, and mini projector were manually mounted and rigidly fixed to ensure a stable geometric configuration throughout the experiment. The specimen, vinyl grating adhered to a rigid MDF plate, was attached to a metallic minicomputer numerical control (CNC) structure that allows controlled horizontal translation, simulating lateral displacement along the *x*-axis, as illustrated in Fig. 4.

The projector–camera–specimen alignment was performed manually using a simple and repeatable visual procedure. The specimen was positioned at a projection distance of 1.2–1.3 m. The camera was then placed approximately collinear with the projector optical axis (without obstructing the projection lens) and adjusted until the MDF specimen appeared approximately rectangular in the image, with its edges aligned with the image axes to minimize perspective distortion. The projected grating was subsequently adjusted (position/zoom) until it was visually superimposed on the physical grating. Alignment was considered satisfactory when stable Moiré fringes with uniform spacing and contrast were observed across the ROI under static conditions, with no visible curvature or drift. The projected grating was then manually aligned with the physical grating prior to baseline acquisition, similar to Fig. 3(c).

Once alignment was achieved, a baseline image corresponding to the undisplaced state (zero displacement) was acquired using the standard webcam at a resolution of 1920 × 1080 pixels. This baseline image captures the initial Moiré fringe pattern and defines the reference configuration against which all subsequent displacement measurements are computed. The baseline is stored persistently, allowing the system to resume measurements across sessions without requiring recalibration, provided that the optical setup remains unchanged.

The Moiré pattern generated by the superposition of the physical and projected gratings is present during this acquisition and is used directly for calibration and displacement analysis. This approach is consistent with that in prior studies on Moiré pattern formation at finite observation distances, where image-based measurements were shown to enable the reliable quantification of lateral displacements.[8]

Following baseline acquisition, an ROI was manually defined to isolate the measurement area. The ROI was selected by interactively marking the four corner points of the overlapped grating region displayed on the screen, as depicted in Fig. 5(a). This manual selection criterion was adopted to explicitly isolate the active Moiré interference area from the complex background

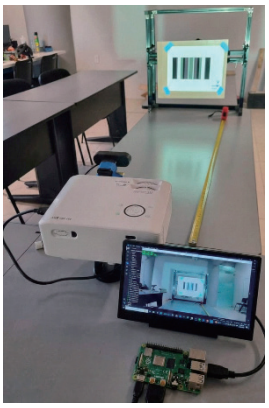

Fig. 4. (Color online) Photograph of the experimental setup used for validation tests, showing the fixed camera–projector configuration and the specimen mounted on a translational structure enabling controlled lateral displacement along the *x*-axis.

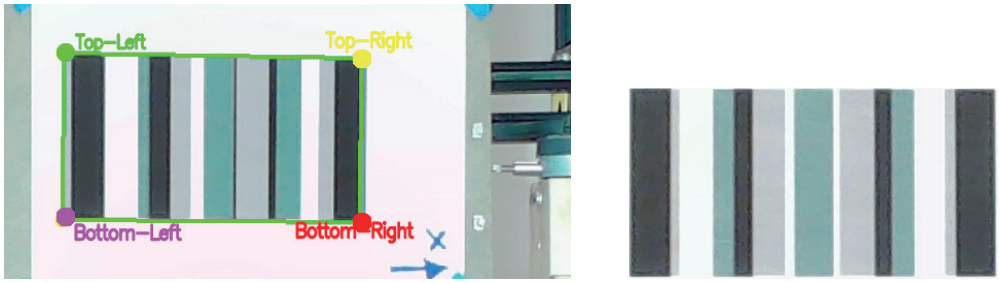

(a) (b)

Fig. 5. (Color online) (a) Reference image acquired in the undeformed state with manual selection of the ROI. (b) Moiré pattern with the defined ROI used as baseline for calibration and displacement tracking.

environment, ensuring that only the relevant fringe data is processed in the subsequent phase correlation analysis without interference from structural elements or uneven lighting outside the grating area.

2.4 Signal processing and displacement estimation

The displacement estimation algorithm processes images in real time to detect lateral shifts between the current frame and the baseline reference. The method is based on one-dimensional phase correlation, which offers robustness against global illumination variations and provides subpixel displacement accuracy. Figure 6 illustrates the complete signal processing and displacement estimation pipeline implemented in the embedded system.

2.4.1 Horizontal profile extraction

For each captured frame, a horizontal intensity profile is extracted by averaging pixel values across the central rows of the rectified image. Given a rectified image $I(x, y)$ of dimensions $W \times H$ pixels, the horizontal profile $P(x)$ is computed as

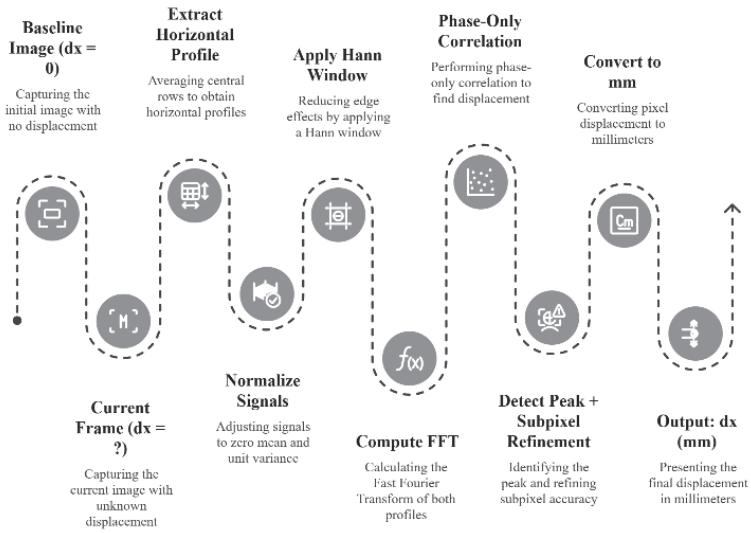

Fig. 6. Diagram of the signal processing algorithm showing the complete workflow from image capture to displacement output.

$$P(x) = (1/N) \times \Sigma\, I(x, y) \text{ for } y \in [y_1, y_2], \tag{2}$$

where $[y_1, y_2]$ defines the central band of rows (typically the middle third of the image) and $N = y_2 - y_1$ is the number of averaged rows. This averaging reduces the effect of local noise while preserving the periodic structure of the Moiré pattern. The resulting profile $P(x)$ is a one-dimensional signal that captures the spatial variation of the interference fringes along the horizontal direction, as shown in Fig. 7.

2.4.2 Phase correlation for shift detection

The displacement between the baseline profile $P_0(x)$ and the current profile $P(x)$ is estimated using phase-only correlation (POC). Both signals are first normalized to zero mean and unit variance to eliminate the effect of global intensity variations:

$$\tilde{P}(x) = [P(x) - \mu] / \sigma, \tag{3}$$

where μ and σ are the mean and standard deviations of the profile, respectively. A Hann window is then applied to both normalized profiles to reduce spectral leakage at the boundaries.

POC is computed by taking the fast Fourier transform (FFT) of both windowed profiles, computing the normalized cross-power spectrum, and applying the inverse FFT:

$$R = IFFT\{[F_0^* \times F] / |F_0^* \times F|\}, \tag{4}$$

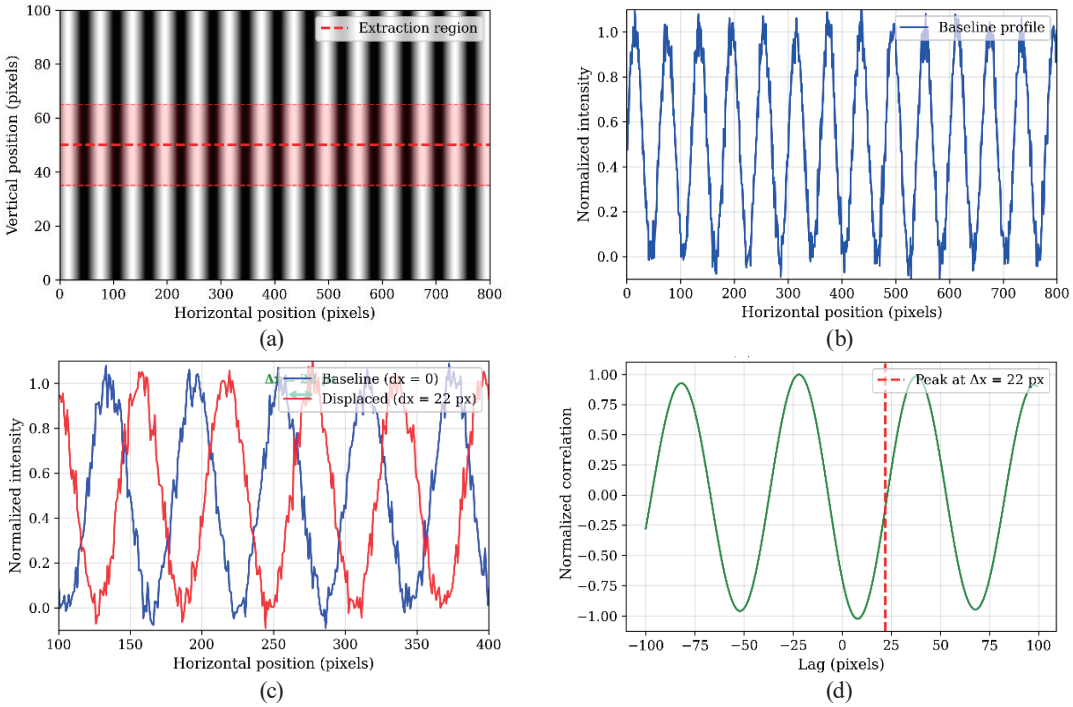

Fig. 7. (Color online) (a) Baseline image showing extraction region. (b) Extracted horizontal profile. (c) Baseline and displaced profiles. (d) Phase correlation result.

where F_0 and F are the Fourier transforms of the baseline and current profiles, respectively, and the asterisk denotes complex conjugation. The displacement in pixels (Δx_{px}) corresponds to the location of the peak in the correlation function R.

2.4.3 Subpixel refinement

To achieve subpixel accuracy, a parabolic interpolation is applied around the correlation peak. Given the peak at integer index k with correlation values $R(k-1)$, $R(k)$, and $R(k+1)$, the subpixel correction δ is computed as

$$\delta = 0.5 \times [R(k-1) - R(k+1)] / [R(k-1) - 2R(k) + R(k+1)]. \quad (5)$$

The refined displacement estimate is then $\Delta x_{px} = k + \delta$.

2.4.4 Conversion to physical units

The pixel displacement is converted to physical units (millimeters) using the spatial calibration factor (mm/px) and the Moiré magnification factor M:

$$\Delta x_{mm} = (\Delta x_{px} \times mm/px) / M. \quad (6)$$

The division by M accounts for the inherent displacement magnification of the Moiré pattern. This relationship allows the system to measure the actual specimen displacement from the amplified fringe shifts observed in the image.

2.4.5 Real-time processing and temporal smoothing

The incoming video frames are continuously processed through the displacement estimation pipeline. While the image rectification and phase correlation algorithms are computationally efficient enough to operate at the camera's native frame rate (typically 15–30 fps on Raspberry Pi 4), the specific nature of quasi-static compression testing allows for temporal aggregation to enhance precision. Consequently, a moving average filter with a window size of 10 s was implemented. This filter is not a computational bottleneck but a deliberate design choice to attenuate high-frequency mechanical vibrations and sensor noise. Therefore, while the underlying processing occurs in real time, the displayed output represents a stabilized measurement optimized for stepwise, static readouts, prioritizing precision over transient dynamic response. Preliminary benchmarks indicate that the Python-based processing pipeline achieves a throughput of approximately 15–20 fps, confirming sufficient capacity for continuous monitoring.

2.5 Calibration procedure

The calibration procedure consists of two stages: automatic spatial calibration to determine the pixel-to-millimeter conversion factor and empirical calibration to correct for deviations between the theoretical and actual Moiré magnification factors.

2.5.1 Automatic spatial calibration (mm/px)

The spatial scale is automatically determined by detecting the period of the physical grating in the captured image. Using the horizontal profile extracted from the baseline image, FFT is used to compute the dominant spatial frequency corresponding to the grating periodicity.

The grating period in pixels (T_{px}) is determined from the location of the dominant peak in the FFT magnitude spectrum, as shown in Fig. 8. Since the physical pitch of the grating is known (p_g = 20 mm), the pixel-to-millimeter conversion factor is computed as

$$mm/px = p_g / T_{px}. \tag{7}$$

This automated approach eliminates manual measurement errors and ensures consistent calibration across experimental sessions. In the present implementation, the detected grating period was 58.99 pixels, yielding a spatial scale of 0.339 mm/px.

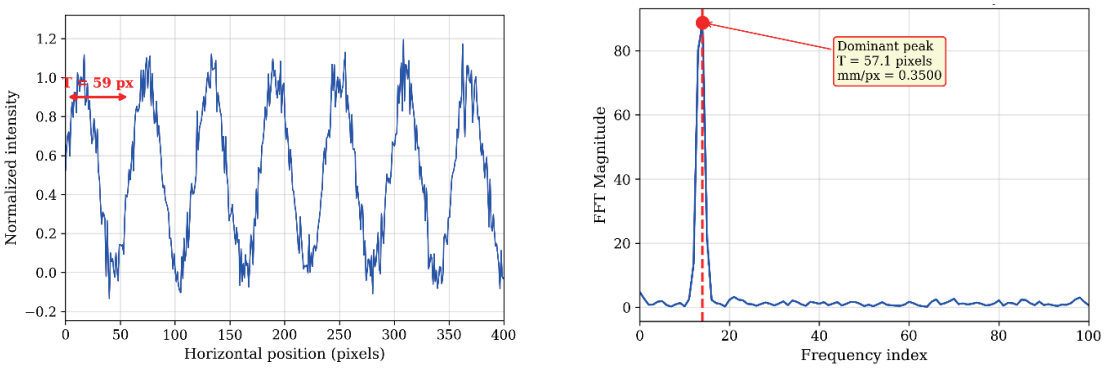

(a) (b)

Fig. 8. (Color online) (a) Horizontal intensity profile showing grating periodicity. (b) FFT spectrum with dominant frequency detection for automatic calibration.

2.5.2 Empirical calibration with known reference

The theoretical Moiré magnification factor (M = 4.33) assumes ideal alignment between the projected and physical gratings. In practice, imperfect alignment, projection geometry variations, and other optical tolerances introduce deviations that affect measurement accuracy. To compensate for these deviations, an empirical calibration procedure is performed using a reference displacement measured by an independent instrument. With the specimen in the baseline position (zero displacement), the system is initialized. The specimen is then translated to a known displacement (d_{ref}), measured using a Mitutoyo digital indicator with 0.001 mm resolution. The system records the corresponding pixel shift (Δx_{px}), and the empirical magnification factor is computed as

$$M_{empirical} = (\Delta x_{px} \times mm/px) / d_{ref}. \tag{8}$$

This empirical factor replaces the theoretical value in Eq. (6) and is stored persistently for subsequent measurements. In the present work, a reference displacement of 5.000 mm was used for empirical calibration, as shown in Fig. 9, ensuring optimal accuracy near the center of the target measurement range. This calibration approach effectively compensates for systematic errors without requiring precise knowledge of the optical geometry.

3. Results

Experimental validation was conducted for lateral displacements in the 0–12 mm range, corresponding to the measurement limits of the digital indicator used as a reference.

3.1 Calibration results

After automated spatial calibration, the system was evaluated for repeatability through 10 independent trials performed consecutively, yielding a mean spatial scale of 0.3388 mm/px with

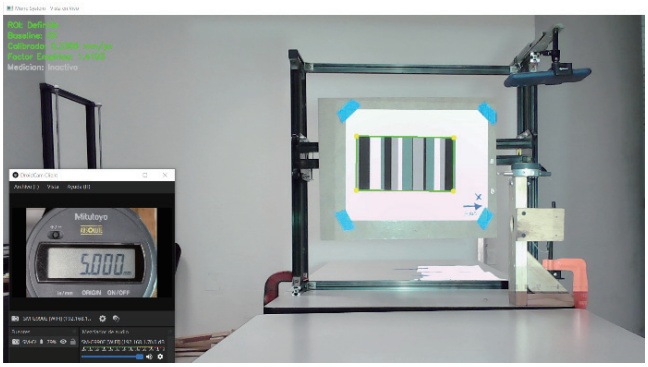

Fig. 9. (Color online) Screenshot of the empirical calibration procedure showing the system interface during reference displacement acquisition (5.000 mm measured with a Mitutoyo digital indicator).

a standard deviation of ±0.0001 mm/px. Regarding the Moiré magnification, the theoretical factor was calculated as M_{theo} = 4.33 from the nominal grating pitches (p_g = 20 mm, p_p = 26 mm). However, the empirical calibration performed at a reference displacement of 5.000 mm revealed an effective magnification factor of M_{emp} = 1.64.

3.2 Displacement measurement validation

The system was validated against a Mitutoyo digital indicator (0.001 mm resolution) over a displacement range of 0–12 mm. Three independent measurement runs were performed at 13 reference positions to assess accuracy and repeatability. The specimen was translated along the *x*-axis using the mini CNC structure, and measurements were recorded after applying the 10 s moving-average filter to ensure signal stabilization.

Table 1 presents experimental results. For each reference position defined by the Mitutoyo indicator, three independent measurements were acquired with the Moiré-based system. The table includes the mean value, standard deviation (as a measure of repeatability), absolute error, and relative error for each measurement point.

3.3 Error values

Figure 10 presents the calibration curve for the Mitutoyo reference values (*x*-axis) against the Moiré system measurements (*y*-axis). The dashed line represents the ideal response ($y = x$), while the data points with error bars show the experimentally measured values with their associated standard deviations. The strong linear correlation confirms the system's capability to track displacement across the tested range, with a Pearson correlation coefficient of R = 0.98.

As illustrated in Fig. 10(c), the relative error is notably higher at small displacements (27.26% at 1 mm) and decreases significantly as displacement increases. For the range of 5–12 mm, the relative error typically remains within the 3–5% range, demonstrating improved relative accuracy in the moderate-to-large displacement regime. The repeatability analysis, illustrated in Fig. 10(d), shows excellent consistency among the three independent measurement runs. The

Table 1
Experimental validation results (three measurement runs).

Mitutoyo (mm)	Run 1 (mm)	Run 2 (mm)	Run 3 (mm)	Mean (mm)	Std dev (mm)	Error (mm)	Error (%)
0.000	0.004	0.002	0.000	0.002	0.0020	0.002	—
1.010	1.285	1.287	1.284	1.285	0.0015	0.275	27.26
2.004	2.004	2.161	2.156	2.107	0.0892	0.103	5.14
3.045	3.116	3.620	3.619	3.452	0.2907	0.407	13.36
4.011	4.315	4.318	4.316	4.316	0.0015	0.305	7.61
5.007	5.005	5.005	5.004	5.005	0.0006	0.002	0.05
6.002	5.723	5.735	5.739	5.732	0.0083	0.270	4.49
7.090	7.203	7.202	7.198	7.201	0.0026	0.111	1.57
8.014	7.920	7.918	7.919	7.919	0.0010	0.095	1.19
9.017	9.316	9.316	9.316	9.316	0.0000	0.299	3.32
10.054	10.029	10.025	10.025	10.026	0.0023	0.028	0.28
11.081	10.701	10.705	10.700	10.702	0.0026	0.379	3.42
12.015	12.186	12.242	12.239	12.222	0.0315	0.207	1.73

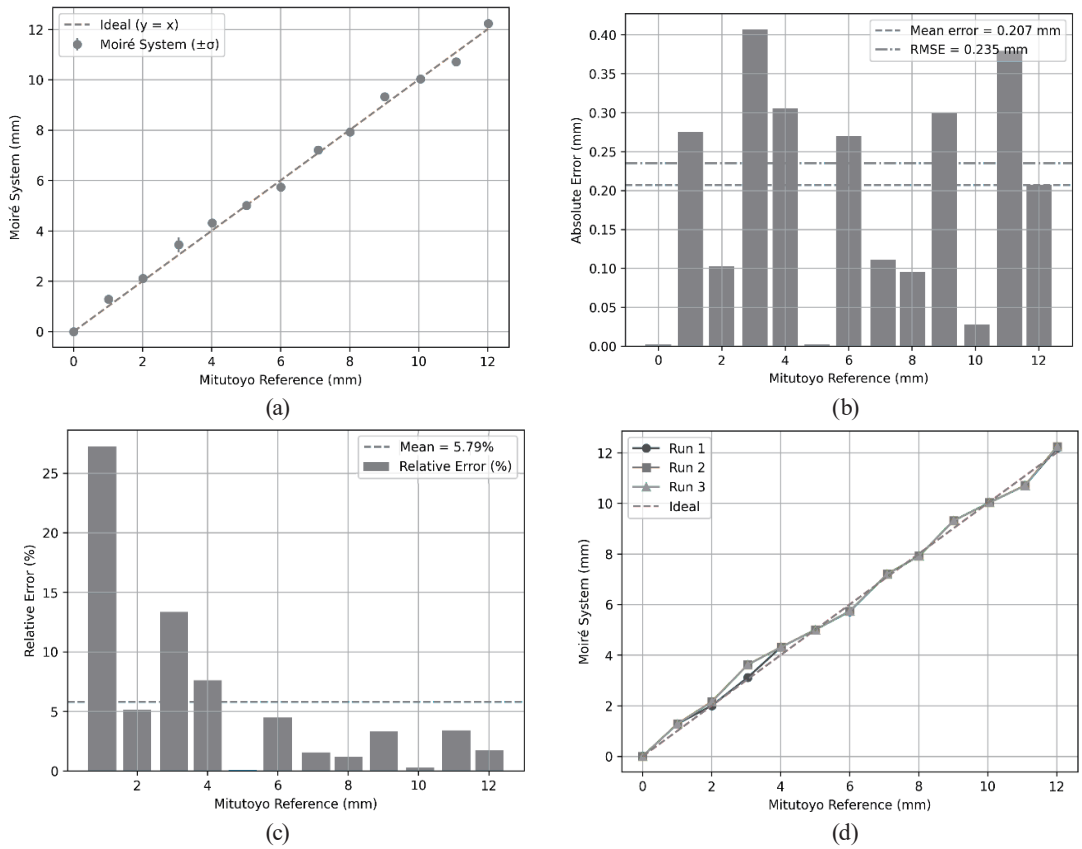

Fig. 10. (a) Calibration curve showing Mitutoyo reference vs Moiré measurement (Pearson coefficient $R = 0.98$). (b) Absolute error vs displacement. (c) Relative error percentage. (d) Overlay of three measurements runs illustrating repeatability.

mean standard deviation of 0.033 mm across all measurement positions indicates that the system produces highly reproducible results under repeated testing conditions. The global error metrics computed from the experimental data are summarized in Table 2.

3.4 Application case: concrete compression testing

To further demonstrate the versatility and ease of deployment of the proposed system under demanding conditions, an additional application case was conducted. The embedded Moiré system was deployed to monitor a standard concrete cylinder compression test using a heavy-duty laboratory press at the Materials Laboratory of the Faculty of Engineering, Universidad Autonoma de Guerrero. As shown in Fig. 11, the active projector, camera, and Raspberry Pi were easily adapted to the industrial frame and successfully tracking the displacement until the ultimate failure (fracture) of the concrete specimen. This test confirms that the low-cost edge-computing architecture is robust enough for harsh experimental environments and can effectively retrofit manual industrial equipment with noncontact optical monitoring capabilities.

Table 2
Global error metrics.

Metric	Value	Unit
Root mean square error (*RMSE*)	0.235	mm
Maximum absolute error	0.407	mm
Mean absolute error (1–12 mm)	0.207	mm
Mean relative error (1–12 mm)	5.79	%
Mean standard deviation	0.033	mm

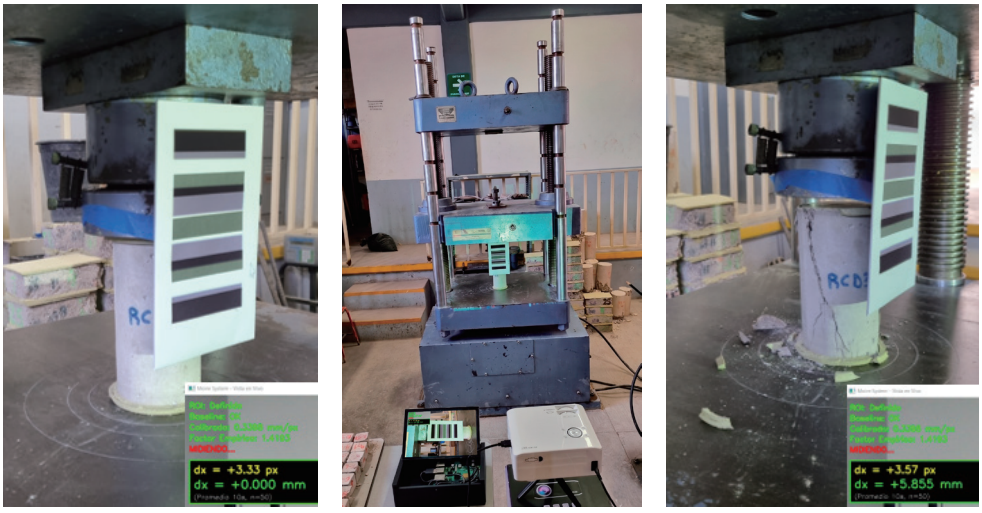

(a) (b) (c)

Fig. 11. (Color online) Validation of the embedded Moiré system in concrete cylinder compression testing. (a) Experimental setup retrofitting a legacy hydraulic laboratory press with the active projection and acquisition units. (b) Details of the active Moiré fringes projected onto the concrete specimen during the loading phase. (c) Specimen after ultimate structural failure (fracture), demonstrating the system's robustness and versatility in harsh experimental environments.

3.5 Cloud data storage and visualization

To validate the remote monitoring capabilities, the displacement data were transmitted asynchronously to the cloud database. Figure 12 shows the developed web-based dashboard interface, where the experimental results—including the unique test ID, timestamp, and the full displacement table—are visualized. The interface allows authorized users to export the dataset in the CSV or PDF format for further offline analysis. This functionality confirms the system's effectiveness as a connected IoT edge node, enabling data accessibility beyond the physical laboratory environment.

4. Discussion

As established, recent sampling Moiré approaches[13,14] provide an essential benchmark for high-precision metrology, achieving sub-micrometer measurements using industrial cameras and controlled lighting. From a strict metrological perspective, these methods clearly outperform the resolution obtained in this study. Consequently, the proposed system is not intended to compete with such precision. Instead, its contribution lies in a deliberate engineering trade-off to democratize optical metrology. By utilizing active projection to overcome uneven ambient lighting, and leveraging low-cost consumer hardware, Raspberry Pi edge-computing, and IoT connectivity, the system provides an accessible pathway to retrofit legacy manual testing machines. This architecture prioritizes affordability, remote monitoring, and ease of deployment in resource-limited educational environments over absolute optical resolution.

The strong linear relationship observed between the Mitutoyo reference displacement and the Moiré-based measurements (R = 0.98) indicates that the system maintains a monotonic response throughout the investigated 0–12 mm range. The reported mean absolute error (0.207 mm) and

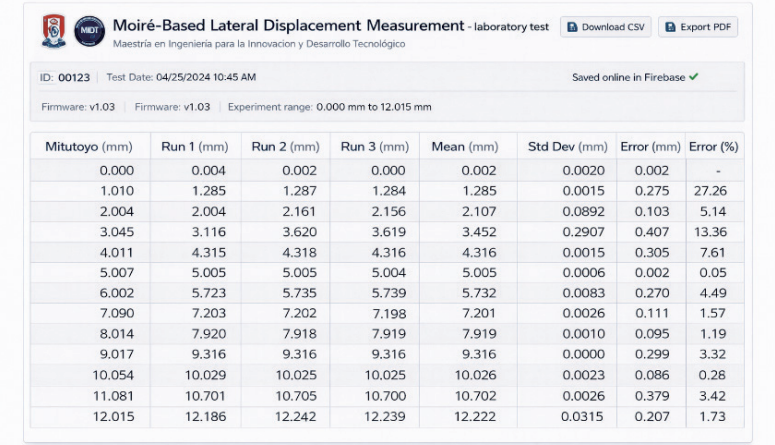

Mitutoyo (mm)	Run 1 (mm)	Run 2 (mm)	Run 3 (mm)	Mean (mm)	Std Dev (mm)	Error (mm)	Error (%)
0.000	0.004	0.002	0.000	0.002	0.0020	0.002	-
1.010	1.285	1.287	1.284	1.285	0.0015	0.275	27.26
2.004	2.004	2.161	2.156	2.107	0.0892	0.103	5.14
3.045	3.116	3.620	3.619	3.452	0.2907	0.407	13.36
4.011	4.315	4.318	4.316	4.316	0.0015	0.305	7.61
5.007	5.005	5.005	5.004	5.005	0.0006	0.002	0.05
6.002	5.723	5.735	5.739	5.732	0.0083	0.270	4.49
7.090	7.203	7.202	7.198	7.201	0.0026	0.111	1.57
8.014	7.920	7.918	7.919	7.919	0.0010	0.095	1.19
9.017	9.316	9.316	9.316	9.316	0.0000	0.299	3.32
10.054	10.029	10.025	10.025	10.026	0.0023	0.086	0.28
11.081	10.701	10.705	10.700	10.702	0.0026	0.379	3.42
12.015	12.186	12.242	12.239	12.222	0.0315	0.207	1.73

Fig. 12. (Color online) Screenshot of web-based dashboard interface showing the synchronized experimental data stored in the Firebase cloud database, including options for CSV and PDF export.

RMSE (0.235 mm) reflect sub-millimeter agreement within the moderate displacement regime considered in this study.

A key implication of these results is that the proposed system must be assessed according to its intended application paradigm. For high-precision full-field deformation analysis—especially when the objective is microscale or strain-resolved measurement under highly controlled lighting—recent phase-based sampling Moiré methods remain the gold standard. By contrast, for moderate displacement monitoring in educational or resource-constrained environments, the present architecture provides a highly strategic engineering compromise. By trading absolute sub-micrometer precision for extreme affordability, active projection (which mitigates uneven ambient lighting), and IoT edge-computing, the system offers a viable, out-of-the-box solution to retrofit legacy manual testing equipment into modern, cloud-connected platforms.

As expected from the empirical calibration procedure, the reference point at 5.000 mm exhibits negligible error, since this displacement was used to determine the effective magnification factor. Consequently, deviations at other positions primarily reflect the combined effect of optical configuration, image acquisition, and signal processing rather than calibration offset.

A relevant outcome of the calibration stage is the discrepancy between the theoretical Moiré magnification factor ($M_{theo} \approx 4.33$), derived from nominal grating pitches, and the experimentally obtained value ($M_{emp} \approx 1.64$). The theoretical model assumes ideal parallel projection and precise pitch matching, whereas the present configuration involves divergent projection optics and manual alignment. Under such nonideal geometric conditions, deviations from the simplified analytical formulation are plausible. The empirical calibration procedure compensates for these effects by directly relating the measured pixel shift to a known physical displacement, allowing the effective magnification factor to represent the actual optical geometry of the system.

The analysis of the error distribution suggests two operating regimes. For displacements below 2 mm, the relative error increases, exceeding 30% near 1 mm. Additional measurements in the 0.8–1.2 mm interval indicate a consistent deviation trend in this low-magnitude range. In this regime, the apparent motion corresponds to pixels in the image domain. Specifically, on the basis of the spatial calibration (0.339 mm/px) and empirical magnification ($M_{emp} \approx 1.64$), a single-pixel shift corresponds to a theoretical limit of detection (LOD) of approximately 0.207 mm. Although subpixel estimation is applied, baseline sensor quantization and symmetric interpolation errors constrain practical sensitivity, preventing the measurement error from reaching zero at these scales.[10] Consequently, an algorithmic uncertainty of just ±1 pixel inherently translates to the observed high relative error near 1 mm. Since image-based measurements are inherently constrained by spatial sampling, and subpixel estimation becomes increasingly sensitive to noise when fringe shifts are small, the observed behavior is consistent with resolution-related limitations reported in Moiré- and vision-based systems.[12,16]

As the displacement magnitude increases, the system transitions to a regime in which the amplified fringe motion improves the effective signal-to-noise ratio. For displacements between 5 and 12 mm, the relative error typically remains below 5%. This range corresponds to displacement levels commonly encountered in quasi-static compression testing, indicating that the system's performance aligns with the intended application scope.

The repeatability of the measurements is supported by the low mean standard deviation of 0.033 mm observed across repeated runs. This dispersion suggests stable behavior under repeated testing conditions. The 10 s moving-average filter contributes to measurement stabilization by attenuating transient disturbances while remaining compatible with the low loading rates characteristic of quasi-static experiments.

Within the broader context of low-cost optical metrology, it is useful to distinguish between full-field displacement analysis and targeted displacement tracking. Open-source DIC frameworks[18,19] enable high-spatial-density strain and displacement mapping, typically relying on subset-based correlation algorithms and greater computational demand. Low-cost implementations for structural or geotechnical applications, such as that described in Ref. 20, demonstrate the feasibility of economical vision-based systems but may involve additional hardware complexity depending on the measurement objective.

In contrast, the present approach focuses on one-dimensional lateral displacement estimation using the optical magnification provided by the Moiré effect. Rather than maximizing spatial density, the system emphasizes moderate-range displacement tracking with reduced hardware cost and embedded real-time processing capability. This positioning reflects a different design objective rather than a direct performance comparison with full-field DIC methods.

Additionally, the embedded architecture incorporates asynchronous cloud-based data logging for remote monitoring, as described in the system overview. Although this functionality does not affect the displacement estimation algorithm, it enables remote supervision and data storage within distributed laboratory environments.

Overall, the results indicate that an embedded active Moiré configuration can provide repeatable displacement measurements within a moderate range when empirical calibration and appropriate signal conditioning are applied. The limitations observed in the low-displacement regime should be considered when defining the intended measurement scope.

5. Conclusions

We presented a compact, affordable (<USD 240) embedded system for noncontact lateral displacement measurement based on active Moiré patterns, on-board image processing, and IoT-enabled remote monitoring. The experimental validation confirmed that the system achieves a linear response ($R = 0.98$) and sub-millimeter accuracy ($MAE = 0.207$ mm) within the moderate 0–12 mm displacement range typical of quasi-static compression testing.

In summary, this research contributes an embedded and connected measurement platform rather than a new high-precision Moiré algorithm. Its relevance lies in demonstrating that practical optical metrology can be implemented with affordable components and edge-to-cloud capabilities for moderate-range testing applications.

Beyond the technical validation, the significance of this work lies in the democratization of optical metrology. By demonstrating that reliable displacement tracking and remote data logging are achievable using consumer-grade electronics and a reference-based empirical calibration, this research bridges the gap between high-end, inaccessible instrumentation and the practical needs of educational and resource-constrained laboratories. The proposed methodology proves

that rigorous measurement capabilities need not be tethered to expensive proprietary hardware and provides a scalable blueprint for open-source instrumentation in experimental mechanics.

Acknowledgments

The authors gratefully acknowledge the support provided by the Faculty of Engineering at the Universidad Autonoma de Guerrero (UAGro) and the Master's in Engineering for Innovation and Technological Development (MIIDT) program.

References

1 N. Daras, T. J. Cloete, and G. N. Nurick: J. Braz. Soc. Mech. Sci. Eng. **46** (2024) 466. https://doi.org/10.1007/s40430-024-05038-y
2 Z. Wang, W. Du, and B. M. Lehane: Acta Geotech. **19** (2024) 651. https://doi.org/10.1007/s11440-023-01977-3
3 P. Vacher, S. Dumoulin, F. Morestin, and S. Mguil-Touchal: Proc. Inst. Mech. Eng. C **213** (1999) 811. https://doi.org/10.1243/0954406991522428
4 F. Hild, B. Raka, M. Baudequin, S. Roux, and F. Cantelaube: Appl. Opt. **41** (2002) 6815. https://doi.org/10.1364/AO.41.006815
5 G. N. Eichhorn, A. Bowman, S. K. Haigh, and S. Stanier: Strain **56** (2020) e12348. https://doi.org/10.1111/str.12348
6 V. Belloni, R. Ravanelli, A. Nascetti, M. Di Rita, D. Mattei, and M. Crespi: Sensors **19** (2019) 3832. https://doi.org/10.3390/s19183832
7 Z. Jiang: Opt. Lasers Eng. **165** (2023) 107566. https://doi.org/10.1016/j.optlaseng.2023.107566
8 V. Saveljev and S.-K. Kim: Opt. Express **20** (2012) 2163. https://doi.org/10.1364/OE.20.002163
9 Q. Wang, S. Ri, and H. Tsuda: Appl. Opt. **55** (2016) 6858. https://doi.org/10.1364/AO.55.006858
10 C. Chen, F. Mao, and J. Yu: Appl. Opt. **60** (2021) 1232. https://doi.org/10.1364/AO.413778
11 J. J. Dirckx: J. Biomed. Opt. **2** (1997) 176. https://doi.org/10.1117/12.268966
12 V. Saveljev and G. Heo: Appl. Mech. **6** (2025) 66. https://doi.org/10.3390/applmech6030066
13 S. Ri, M. Fujigaki, and Y. Morimoto: Exp. Mech. **50** (2010) 501. https://doi.org/10.1007/s11340-009-9239-4
14 Q. Wang and S. Ri: Theor. Appl. Mech. Lett. **12** (2022) 100327. https://doi.org/10.1016/j.taml.2022.100327
15 J. Schlobohm, A. Pösch, and E. Reithmeier: Electronics **5** (2016) 43. https://doi.org/10.3390/electronics5030043
16 M. Wang, K.-Y. Koo, C. Liu, and F. Xu: Eng. Struct. **278** (2023) 115493. https://doi.org/10.1016/j.engstruct.2022.115493
17 M. Wang, F. Xu, K.-Y. Koo, and P. Wang: Comput.-Aided Civ. Infrastruct. Eng. **39** (2024) 1988. https://doi.org/10.1111/mice.13177
18 D. Turner, P. Crozier, and P. Reu: DOE CODE (2015) 3620. https://doi.org/10.11578/dc.20171025.1658
19 J. Blaber, B. Adair, and A. Antoniou: Exp. Mech. **55** (2015) 1105. https://doi.org/10.1007/s11340-015-0009-1
20 V. Nezerka and P. Havlasek: Exp. Tech. **46** (2022) 485. https://doi.org/10.1007/s40799-021-00488-8